The Astrophysical Journal, 779:27 (10pp), 2013 December 10 doi:10.1088/0004-637X/779/1/27

TeV GAMMA-RAY SURVEY OF THE NORTHERN SKY USING THE ARGO-YBJ DETECTOR

B. Bartoli[1,2], P. Bernardini[3,4], X. J. Bi[5], I. Bolognino[6,7], P. Branchini[8], A. Budano[8], A. K. Calabrese Melcarne[9], P. Camarri[10,11], Z. Cao[5], R. Cardarelli[11], S. Catalanotti[1,2], S. Z. Chen[5], T. L. Chen[12], Y. Chen[5], P. Creti[4], S. W. Cui[13], B. Z. Dai[14], A. D'Amone[3,4], Danzengluobu[12], I. De Mitri[3,4], B. D'Ettorre Piazzoli[1,2], T. Di Girolamo[1,2], X. H. Ding[12], G. Di Sciascio[11], C. F. Feng[15], Zhaoyang Feng[5], Zhenyong Feng[16], Q. B. Gou[5], Y. Q. Guo[5], H. H. He[5], Haibing Hu[12], Hongbo Hu[5], Q. Huang[16], M. Iacovacci[1,2], R. Iuppa[10,11], H. Y. Jia[16], Labaciren[12], H. J. Li[12], J. Y. Li[15], X. X. Li[5], G. Liguori[6,7], C. Liu[5], C. Q. Liu[14], J. Liu[14], M. Y. Liu[12], H. Lu[5], L. L. Ma[5], X. H. Ma[5], G. Mancarella[3,4], S. M. Mari[8,17], G. Marsella[3,4], D. Martello[3,4], S. Mastroianni[2], P. Montini[8,17], C. C. Ning[12], M. Panareo[3,4], B. Panico[10,11], L. Perrone[3,4], P. Pistilli[8,17], F. Ruggieri[8], P. Salvini[7], R. Santonico[10,11], S. N. Sbano[3,4], P. R. Shen[5], X. D. Sheng[5], F. Shi[5], A. Surdo[4], Y. H. Tan[5], P. Vallania[18,19], S. Vernetto[18,19], C. Vigorito[19,20], B. Wang[5], H. Wang[5], C. Y. Wu[5], H. R. Wu[5], B. Xu[16], L. Xue[15], Q. Y. Yang[14], X. C. Yang[14], Z. G. Yao[5], A. F. Yuan[12], M. Zha[5], H. M. Zhang[5], Jilong Zhang[5], Jianli Zhang[5], L. Zhang[14], P. Zhang[14], X. Y. Zhang[15], Y. Zhang[5], J. Zhao[5], Zhaxiciren[12], Zhaxisangzhu[12], X. X. Zhou[16], F. R. Zhu[16], Q. Q. Zhu[5], and G. Zizzi[9]

(The ARGO-YBJ Collaboration)

[1] Dipartimento di Fisica dell'Università di Napoli "Federico II," Complesso Universitario di Monte Sant'Angelo, via Cinthia, I-80126 Napoli, Italy
[2] Istituto Nazionale di Fisica Nucleare, Sezione di Napoli, Complesso Universitario di Monte Sant'Angelo, via Cinthia, I-80126 Napoli, Italy
[3] Dipartimento Matematica e Fisica "Ennio De Giorgi," Università del Salento, via per Arnesano, I-73100 Lecce, Italy
[4] Istituto Nazionale di Fisica Nucleare, Sezione di Lecce, via per Arnesano, I-73100 Lecce, Italy
[5] Key Laboratory of Particle Astrophysics, Institute of High Energy Physics, Chinese Academy of Sciences, P.O. Box 918, 100049 Beijing, China; chensz@ihep.ac.cn
[6] Dipartimento di Fisica dell'Università di Pavia, via Bassi 6, I-27100 Pavia, Italy
[7] Istituto Nazionale di Fisica Nucleare, Sezione di Pavia, via Bassi 6, I-27100 Pavia, Italy
[8] Istituto Nazionale di Fisica Nucleare, Sezione di Roma Tre, via della Vasca Navale 84, I-00146 Roma, Italy
[9] Istituto Nazionale di Fisica Nucleare - CNAF, Viale Berti-Pichat 6/2, I-40127 Bologna, Italy
[10] Dipartimento di Fisica dell'Università di Roma "Tor Vergata," via della Ricerca Scientifica 1, I-00133 Roma, Italy
[11] Istituto Nazionale di Fisica Nucleare, Sezione di Roma Tor Vergata, via della Ricerca Scientifica 1, I-00133 Roma, Italy
[12] Tibet University, 850000 Lhasa, Xizang, China
[13] Hebei Normal University, Shijiazhuang 050016, Hebei, China
[14] Yunnan University, 2 North Cuihu Rd., 650091 Kunming, Yunnan, China
[15] Shandong University, 250100 Jinan, Shandong, China
[16] Southwest Jiaotong University, 610031 Chengdu, Sichuan, China
[17] Dipartimento di Fisica dell'Università "Roma Tre," via della Vasca Navale 84, I-00146 Roma, Italy
[18] Osservatorio Astrofisico di Torino dell'Istituto Nazionale di Astrofisica, corso Fiume 4, I-10133 Torino, Italy
[19] Istituto Nazionale di Fisica Nucleare, Sezione di Torino, via P. Giuria 1, I-10125 Torino, Italy
[20] Dipartimento di Fisica dell'Università di Torino, via P. Giuria 1, I-10125 Torino, Italy

Received 2013 August 12; accepted 2013 October 11; published 2013 November 22

ABSTRACT

The Astrophysical Radiation with Ground-based Observatory at Yang Ba Jing (ARGO-YBJ) detector is an extensive air shower array that has been used to monitor the northern γ-ray sky at energies above 0.3 TeV from 2007 November to 2013 January. In this paper, we present the results of a sky survey in the declination band from -10° to 70°, using data recorded over the past five years. With an integrated sensitivity ranging from 0.24 to $\sim$1 Crab units depending on the declination, six sources have been detected with a statistical significance greater than five standard deviations. Several excesses are also reported as potential γ-ray emitters. The features of each source are presented and discussed. Additionally, 95% confidence level upper limits of the flux from the investigated sky region are shown. Specific upper limits for 663 GeV γ-ray active galactic nuclei inside the ARGO-YBJ field of view are reported. The effect of the absorption of γ-rays due to the interaction with extragalactic background light is estimated.

Key words: gamma rays: general – surveys

Online-only material: color figures

1. INTRODUCTION

Over the past two decades, great advances have been made in very high energy (VHE) γ-ray astronomy and almost 150 sources have been observed by ground-based γ-ray detectors. Several categories of VHE γ-ray emitters have been firmly established: active galactic nuclei (AGNs), pulsar wind nebulae (PWNs), supernova remnants (SNRs), X-ray binaries (XBs), and starburst galaxies. VHE γ-ray astronomy, therefore, has progressively introduced new ways to probe the non-thermal universe and the extreme physical processes in astrophysical sources. VHE γ-rays are emitted by relativistic particles accelerated at the astrophysical shocks that are widely believed to exist in all VHE sources. These shocks may accelerate protons or electrons. Relativistic electrons can scatter low energy photons to VHE levels via the inverse Compton process, while relativistic protons would lead to hadronic cascades and VHE γ-rays are generated by the decay of secondary π^0 mesons. Hence, VHE γ-ray observations are also important for understanding the origin and acceleration of cosmic rays.

VHE γ-ray emitters include Galactic sources and extragalactic sources. Most of the identified Galactic sources belong to PWNs, SNRs, and XBs; however, about one-third of them are still unidentified.[21] Extragalactic sources are mainly composed of blazars, including BL-Lac-type objects and flat spectrum radio quasars (FSRQs). Due to interaction with extragalactic background light (EBL), which causes a substantial reduction of the flux, VHE γ-ray observations are limited to nearby sources. The most distant VHE source located to date is 3C 279 with a redshift value of $z = 0.536$ (Albert et al. 2008a).

Recent advances in the observation of VHE γ-rays are mainly attributed to the successful operation of imaging atmospheric Cherenkov telescopes (IACTs), such as H.E.S.S., MAGIC, VERITAS, and CANGAROO, which made a majority of the discoveries when searching for counterparts of sources observed at lower energies (for a review, see Aharonian et al. 2008c). To achieve an overall view of the universe in the VHE γ-ray band, an unbiased sky survey is needed, similar to that carried out by *Fermi* and its predecessor EGRET at GeV energies. The two surveys detected 1873 and 271 objects, respectively, including 575 and 170 sources still unidentified (Nolan et al. 2012; Hartman et al. 1999). The H.E.S.S. collaboration has made great progress in surveying the Galactic plane and has revealed over 60 new VHE γ-ray sources (Gast et al. 2011). However, due to their small fields of view (FOVs) and low duty cycles, IACTs are not suitable for performing a long-term comprehensive sky survey. Although, with a sensitivity lower than that of IACTs, extensive air shower (EAS) arrays, such as Tibet ASγ, Milagro, and Astrophysical Radiation with Ground-based Observatory at Yang Ba Jing (ARGO-YBJ), are the only choices available for performing a continuous sky survey of VHE sources. To date, several surveys have been performed by AIROBICC (Aharonian et al. 2002), Milagro (Atkins et al. 2004), and Tibet ASγ (Amenomori et al. 2005). The latter two surveys have resulted in the successful observation of γ-ray emissions from the Crab Nebula and Mrk 421. The best upper limits at energies above 1 TeV are around 0.27−0.60 Crab units achieved by the Milagro experiment. In 2007, Milagro updated its survey of the Galactic plane and three new extended sources were discovered (Abdo et al. 2007). Additionally, both Milagro and ASγ have observed some excesses from positions associated with the *Fermi* Bright Source List inside the Galactic plane (Abdo et al. 2009; Amenomori et al. 2010).

The ARGO-YBJ detector is an EAS array with a large FOV and can continuously monitor the sky in the declination band from -10° to 70°. With its full coverage configuration and its location at a high altitude of 4300 m a.s.l., the energy threshold of ARGO-YBJ is much lower than that of any previous EAS array. Since the γ-ray absorption due to EBL increases with the γ-ray energy, ARGO-YBJ, working with a threshold of a few hundred GeV, is suitable for observing AGNs that account for 80% of the known γ-ray sources as revealed by *Fermi* (Nolan et al. 2012). Previously, the ARGO-YBJ collaboration reported the search for emission of GeV-TeV photons from gamma-ray bursts (Aielli et al. 2009a, 2009c) and the observation of flaring activity from AGNs (Bartoli et al. 2011a, 2012b), and specific observations for extended sources inside the Galactic plane (Bartoli et al. 2012a, 2012c, 2013). This paper presents the analysis of a sky survey that searched for steady VHE γ-ray emitters using more than five years of data collected by ARGO-YBJ.

[21] http://tevcat.uchicago.edu/ (Version: 3.400, as of 2013 July).

2. THE ARGO-YBJ DETECTOR

The ARGO-YBJ detector, located at the Yangbajing Cosmic Ray Observatory (Tibet, China, 90.°5 east, 30.°1 north), is designed for VHE γ-ray astronomy and cosmic-ray observations. It consists of a single layer of Resistive Plate Chambers (RPCs; 2.8 m × 1.25 m) equipped with 10 logical pixels (called pads, 55.6 cm × 61.8 cm each) used for triggering and timing purposes. One-hundred and thirty clusters (each composed of 12 RPCs) are installed to form the central carpet of 74 m × 78 m with an active area of ∼92%, surrounded by 23 additional partially instrumented clusters (the "guard ring"). The total area of the array is 110 m × 100 m. Further details about the detector and the RPC performance can be found in Aielli et al. (2006, 2009d). The arrival time of a particle is measured with a resolution of approximately 1.8 ns. In order to calibrate the 18,360 Time to Digital Converter channels, we have developed a method using cosmic ray showers (He et al. 2007). The calibration precision is 0.4 ns and the procedure is applied every month (Aielli et al. 2009b).

The central 130 clusters began recording data in 2006 July, while the "guard ring" was merged into the Data Acquisition stream in 2007 November. The ARGO-YBJ detector is operated by requiring the coincidence of at least 20 fired pads ($N_{\rm pad}$) within 420 ns on the entire carpet detector. The time of each fired pad in a window of 2 μs around the trigger time and its location are recorded. The trigger rate is 3.5 kHz with a dead time of 4% and the average duty-cycle is higher than 86%.

The high granularity of the apparatus permits a detailed space-time reconstruction of the shower profile, including the shower core and incident direction of the primary particle. The shower core is estimated using a maximum likelihood method by fitting the lateral density distribution of the shower with an Nishimura-Kamata-Greisen–like function. The core resolution (68% containment) is better than 10 m for events with $N_{\rm pad}$ >100, and worsens for events with fewer pads. The incident direction is reconstructed using the least squares method assuming a conical shape of the shower front. The conical correction coefficient defined in Equation (1) of Aielli et al. (2009b), which describes the increase of time delay with the distance to the shower core, is fixed at 0.1 ns m^{-1}. According to Eckmann et al. (1991), a systematic inclination of the reconstructed shower direction exists if the shower core is near the edge of the detector array. The effect has been confirmed using ARGO-YBJ simulation data samples and has been corrected using the method presented in Eckmann et al. (1991). This correction has little effect for events with $N_{\rm pad} < 100$ due to the large uncertainty in the core location, while it can improve the angular resolution for events with $N_{\rm pad} > 200$ by ∼20%. The improvement is better at higher multiplicities.

To improve the sensitivity for γ-ray source observation, an optimization on the selection of the shower core position is applied. The event selections are listed in Table 1, where R is the distance between the shower core position and the carpet center, and TS is the time spread of the shower front in the conical fit defined in Equation (1) of Aielli et al. (2009b). With these selections, more background cosmic rays than γ-rays are rejected and the corresponding angular resolutions are also improved. Therefore, the sensitivity is improved by 10%–30% with respect to that with no event selection for a Crab-like source in different $N_{\rm pad}$ ranges. The angular resolution ($\sigma_{\rm res}$) for events with different multiplicities is listed in Table 1. The point-spread function (PSF) is fitted using a symmetrical

Table 1
Event Selections and Number of Events

N_{pad} Range	R (m)	TS (ns^2)	σ_{res} (deg)	Median Energy (TeV)	Number of Events ($\times 10^9$)	Surviving Fraction (%)
[20, 40]	No cut	<80	1.66	0.36	128	73.0
[40, 60]	No cut	<80	1.34	0.56	102	74.2
[60, 100]	<90	<80	0.94	0.89	39.3	53.4
[100, 130]	<70	<80	0.71	1.1	8.87	45.1
[130, 200]	<65	<80	0.58	1.4	8.62	43.9
[200, 500]	<60	<80	0.42	2.8	8.06	45.9
[500, 1000]	<50	<80	0.31	4.5	2.19	48.8
[1000, 2000]	<40	<80	0.22	8.9	0.806	45.5
[>2000]	<30	<80	0.17	18	0.317	34.7

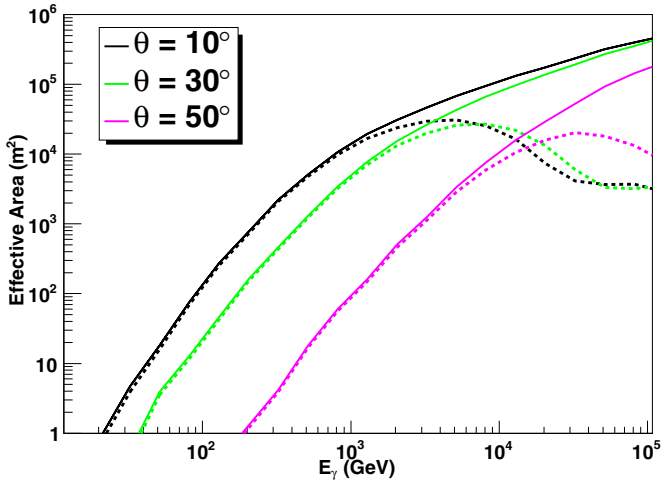

Figure 1. ARGO-YBJ effective areas for γ-rays as a function of the energy for the three zenith angles $\theta = 10^\circ$, $\theta = 30^\circ$, and $\theta = 50^\circ$. The solid lines are obtained with all the triggered events ($N_{pad} \geqslant 20$), while the dotted lines with the selected events as listed in Table 1.

(A color version of this figure is available in the online journal.)

two-dimensional Gaussian function with sigma $= \sigma_{res}$. The angular resolution listed in Table 1 is for a γ-ray shower. The median energies depend on both the γ-ray spectral index and the source declination. The median energies exhibited in Table 1 are for γ-rays from the Crab Nebula.

The effective area of the ARGO-YBJ detector for detecting γ-ray showers is estimated using a full Monte Carlo simulation driven by CORSIKA 6.502 (Capdevielle et al. 1992) and by the GEANT4-based code G4argo (Guo et al. 2010). The core location of the shower is sampled inside an area of 1000 m $\times$ 1000 m around the carpet center. The effective areas for γ-rays at the three zenith angles $\theta = 10^\circ$, $\theta = 30^\circ$, and $\theta = 50^\circ$ are shown in Figure 1 as a function of the primary energy from 10 GeV to 100 TeV. The solid lines are for all triggered events with $N_{pad} > 20$. The dotted lines show the effective areas after applying the selections listed in Table 1. The effective area is about 100 m^2 at 100 GeV and ~10,000 m^2 above 1 TeV for a zenith angle of 10°.

The performance of the ARGO-YBJ detector array has been thoroughly tested by measuring the cosmic ray shadow cast by the Moon and the Sun (Bartoli et al. 2011b; Aielli et al. 2011). The angular resolution obtained using the Moon shadow test is in good agreement with the Monte Carlo simulation. The position of the shadow allows for the investigation of any pointing bias. The east–west displacement is in good agreement with the expectation, while a 0.°1 pointing error toward the north is observed. By studying the westward shift of the shadow due to the geomagnetic field, the total absolute energy scale error, including systematic effects, is estimated to be less than 13% (Bartoli et al. 2011b).

3. DATA ANALYSIS

The ARGO-YBJ data used in this analysis was collected from 2007 November to 2013 January. The total effective observation time is 1670.45 days. For the analysis presented in this paper, only events with zenith angles less than 50° are used, and data sets are divided into nine groups according to the number of N_{pad} firing. The event selections listed in Table 1 are applied. The number of events in each group and the fraction of selected events are also listed in Table 1. The number of events used in this work is 2.99×10^{11}, which is 66.4% of the total number of events recorded at zenith angles <50°.

For the data set in each group, the sky map in celestial coordinates (right ascension and declination) is divided into a grid of 0.°1 $\times$ 0.°1 bins and filled with detected events according to their reconstructed arrival direction. The number of events is denoted as n. To obtain the excess of γ-induced showers in each bin, the "direct integral method" (Fleysher et al. 2004) is adopted in order to estimate the number of cosmic ray background events in the bin, denoted as b. To remove the effect of cosmic ray anisotropy on a scale of 11° $\times$ 11°, a correction procedure as described in Bartoli et al. (2011a) has been applied. To reduce the contamination from the Galactic Plane diffuse γ-ray emission, a specific similar correction procedure has been adopted in the region of Galactic latitude $|\ b\ | < 2^\circ$. Diffuse γ-rays are estimated on a scale of 16° $\times$ 4° in Galactic coordinates along the Galactic Plane, and the contribution from a 5° $\times$ 4° window around the source bin is excluded.

In order to extract the γ-ray signals, the events in a circular area centered on the bin within an angular radius of $2\sigma_{res}$ are summed after weighting with the Gaussian-shaped PSF. Each bin is denoted as i. The weight is

$$w(r) = \frac{1}{2\pi\sigma_{res}^2} e^{-r^2/(2\sigma_{res}^2)}, \quad (1)$$

where r is the space angle to the central bin. Equation (9) in Li & Ma (1983) is used to estimate the significance of the excess in each bin. That is,

$$S = \frac{N_s}{\sigma(N_s)}, \quad (2)$$

where

$$N_s = \sum_i w(r)(n_i - b_i),\ \sigma(N_s) = \sqrt{\sum_i w^2(r)(n_i\alpha + b_i)}. \quad (3)$$

Table 2
Location of the Excess Regions

ARGO-YBJ Name	R.A.[a] (deg)	Decl.[a] (deg)	l (deg)	b (deg)	S (s.d.)	Associated TeV Source
ARGO J0409−0627	62.35	−6.45	198.51	−38.73	4.8	
ARGO J0535+2203	83.75	22.05	184.59	−5.67	20.8	Crab Nebula
ARGO J1105+3821	166.25	38.35	179.43	65.09	14.1	Mrk 421
ARGO J1654+3945	253.55	39.75	63.59	38.80	9.4	Mrk 501
ARGO J1839−0627	279.95	−6.45	25.87	−0.36	6.0	HESS J1841−055
ARGO J1907+0627	286.95	6.45	40.53	−0.68	5.3	HESS J1908+063
ARGO J1910+0720	287.65	7.35	41.65	−0.88	4.3	
ARGO J1912+1026	288.05	10.45	44.59	0.20	4.2	HESS J1912+101
ARGO J2021+4038	305.25	40.65	78.34	2.28	4.3	VER J2019+407
ARGO J2031+4157	307.95	41.95	80.58	1.38	6.1	MGRO J2031+41 TeV J2032+4130
ARGO J1841−0332	280.25	−3.55	28.58	0.70	4.2	HESS J1843−033

Note. [a] R.A. and decl. are celestial coordinates in J2000 epoch.

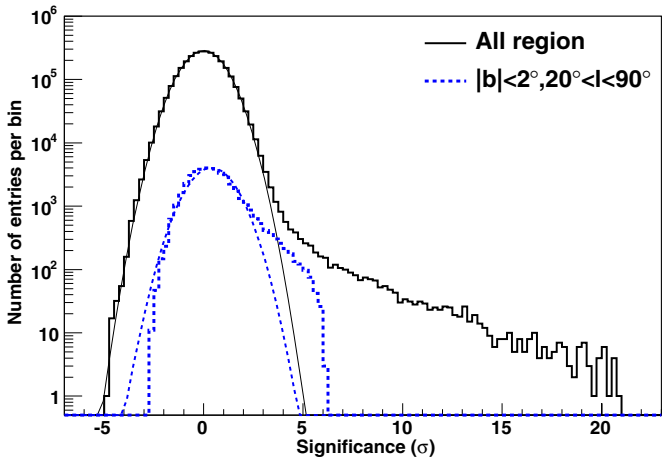

Figure 2. Pre-trial significance distribution for the whole sky map (thick solid line). The thin solid line represents the best Gaussian fit. The significance distribution for the Galactic Plane region with $|\ b\ | < 2^\circ$ and $20^\circ < l < 90^\circ$ is shown by the thick dotted line. The thin dotted line represents the best Gaussian fit for this region.

(A color version of this figure is available in the online journal.)

The quantity α is the ratio of the signal and background exposures (Fleysher et al. 2004). The equation above can be used for both one-group data sets and multi-group data sets. For one-group data, the improvement of the significance compared to the case with $w(r) = 1$ is about 10%. For the nine groups, the improvement is about 40% for the analysis presented in this work, compared with the traditional method of using one average angular radius for all groups.

4. RESULTS

4.1. Sky Survey Results

The pre-trial significance distribution of the bins in the whole map is shown in Figure 2. The distribution, with a mean value of 0.002 and $\sigma = 1.02$, closely follows a standard Gaussian distribution except for a tail with large positive values, due to excesses from several γ-ray emission regions. Figure 3 shows the significance map of the observed sky, in which the positions of the excess regions are visible. Table 2 lists the locations of the regions with significant standard deviations (s.d.) greater than 4.5. For each independent region, only the coordinates of the pixel with the highest significance are given. Based on the distribution of negative values (Figure 2), a significance threshold of 4.5 s.d. corresponds to ∼2 false sources in our catalog.

The Galactic plane is rich in potential γ-ray sources, and many VHE emitters have been detected. Recently, new candidates within the Galactic plane have been reported by Milagro and Tibet ASγ (Abdo et al. 2009; Amenomori et al. 2010). The significance distribution of the inner Galactic plane region (longitude $20^\circ < l < 90^\circ$ and latitude $|\ b\ | < 2^\circ$) is also shown in Figure 2. The Gaussian fit of the distribution has a mean of 0.40 and $\sigma = 1.04$. In this case, due to significant excess, a tail is present. The locations of the excesses with significance greater than 4.0 s.d. are also listed in Table 2. The significance map of the inner Galactic plane region ($20^\circ < l < 90^\circ$, $|b| < 10^\circ$) is shown in Figure 4. For comparison, the known GeV and TeV sources are marked in the figure. Four regions are significantly higher than other regions, i.e., ARGO J1839−0627, ARGO J1907+0627, ARGO J1912+1026, and ARGO J2031+4157. To explore the Galactic plane at different energies, the map obtained using events with $N_{\rm pad} \geqslant 100$ (corresponding to a median energy ∼1.8 TeV) is shown in the bottom panel of Figure 4.

Only pre-trial significances are reported in Table 2. It is very difficult to count the number of trials directly, given that the significances for adjacent grid points are correlated since the smoothing radius is larger than the grid spacing. Since the smoothing radius is larger than the bin width, the significances in adjacent bins are correlated, and a Monte Carlo simulation is necessary to correctly evaluate the post-trial probabilities. According to our simulations, a chance probability less than 5% corresponds to pre-trial significance thresholds as high as 5.1 s.d. anywhere in the map and 4.0 s.d. in the Galactic Plane. However, since only ∼70 known VHE emitters exist in the sky region monitored by ARGO-YBJ, the post-trial significance increases for any candidate source associated with a counterpart.

4.2. Characteristics of Each Source and Source Candidate

In the following, a detailed presentation of the sources and candidates listed in Table 2 is given.

ARGO J0535+2203, detected at 21 s.d., is consistent in position with the Crab Nebula. The location is $0\overset{\circ}{.}08$ from the pulsar, within the statistical error. The spectral energy distribution (SED) derived from the ARGO-YBJ data, using the conventional fitting method described in Bartoli et al. (2011a),

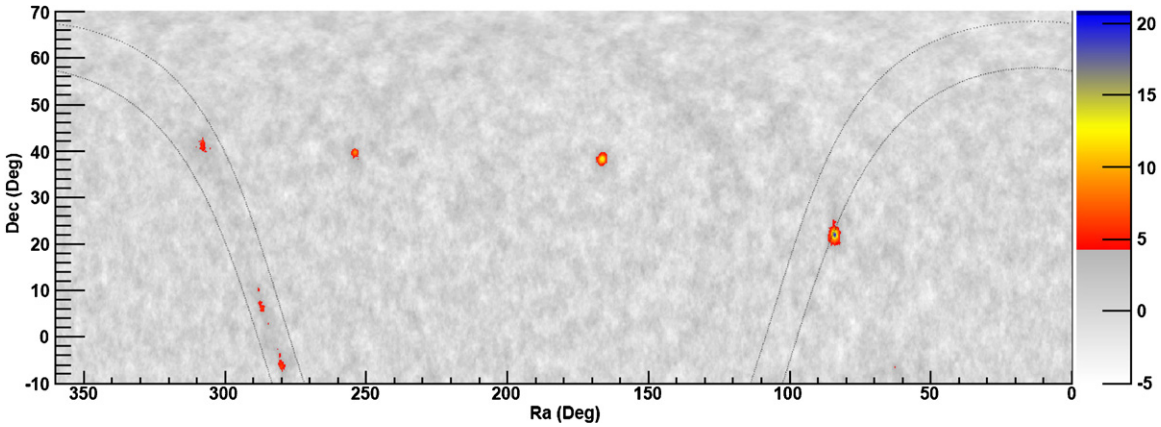

Figure 3. Significance map of the sky as seen by ARGO-YBJ in VHE band. The significances of the excesses, in terms of standard deviations, are shown by the color scale on the right side. The two dotted lines indicate the Galactic latitudes $b = \pm 5^{\circ}$.

(A color version of this figure is available in the online journal.)

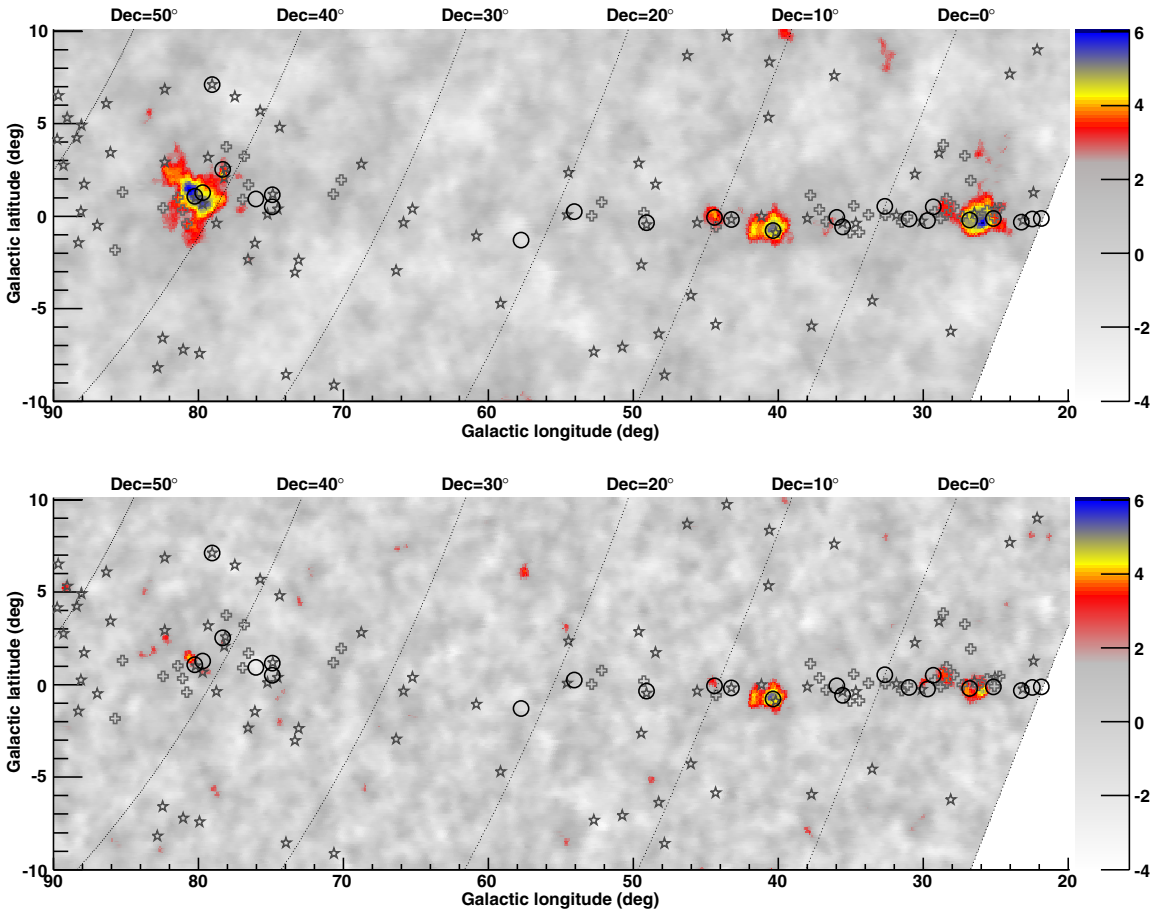

Figure 4. Significance map of the Galactic Plane region with $| b | < 10^{\circ}$ and $20^{\circ} < l < 90^{\circ}$ obtained by the ARGO-YBJ detector. The circles indicate the positions of all the known VHE sources. The open stars mark the locations of the GeV sources in the second *Fermi*-LAT catalog (Nolan et al. 2012). The open crosses mark the locations of the sources considered to be potentially confused with Galactic diffuse emission in the second *Fermi*-LAT catalog (Nolan et al. 2012). The top panel was obtained using ARGO-YBJ events with $N_{\rm pad} \geqslant 20$ (corresponding to a median energy ∼0.7 TeV) while the bottom panel was obtained using events with $N_{\rm pad} \geqslant 100$ (corresponding to a median energy ∼1.8 TeV). The four excess regions are ARGO J1839−0627, ARGO J1907+0627, ARGO J1912+1026, and ARGO J2031+4157.

(A color version of this figure is available in the online journal.)

in the energy range from 0.1 TeV to 35 TeV is $dN/dE = (3.00 \pm 0.18) \times 10^{-11} (E/1\ \mathrm{TeV})^{-2.62 \pm 0.06}$ ($\mathrm{TeV}^{-1}\ \mathrm{cm}^{-2}\ \mathrm{s}^{-1}$). Only statistical errors are listed here. The integral flux of this spectrum is denoted as $I_{\rm crab}$ in the following text. The integral flux above 1 TeV is $1.85 \times 10^{-11}\ \mathrm{cm}^{-2}\ \mathrm{s}^{-1}$. It is $5.69 \times 10^{-11}\ \mathrm{cm}^{-2}\ \mathrm{s}^{-1}$ above 500 GeV. This SED is consistent, within the errors, with the results obtained by other experiments, e.g., HEGRA, H.E.S.S., MAGIC, and Tibet ASγ (Aharonian et al. 2004, 2006; Albert et al. 2008b; Amenomori et al. 2009). A comparison among different experiments is shown in Figure 5. The figure shows only statistical errors. The systematic errors on the flux for point sources have been described in

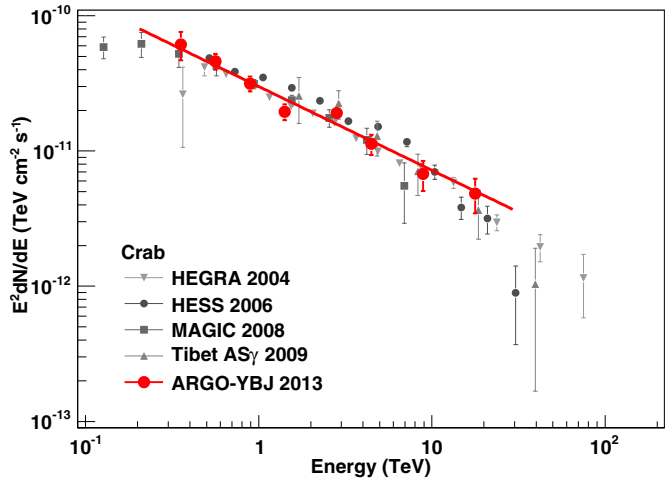

Figure 5. Spectral energy distribution of the Crab Nebula measured by ARGO-YBJ and comparison with the measurements of HEGRA, H.E.S.S., MAGIC, and Tibet ASγ (Aharonian et al. 2004, 2006; Albert et al. 2008b; Amenomori et al. 2009). The solid line is the best fit to the ARGO-YBJ data using a power-law function.

(A color version of this figure is available in the online journal.)

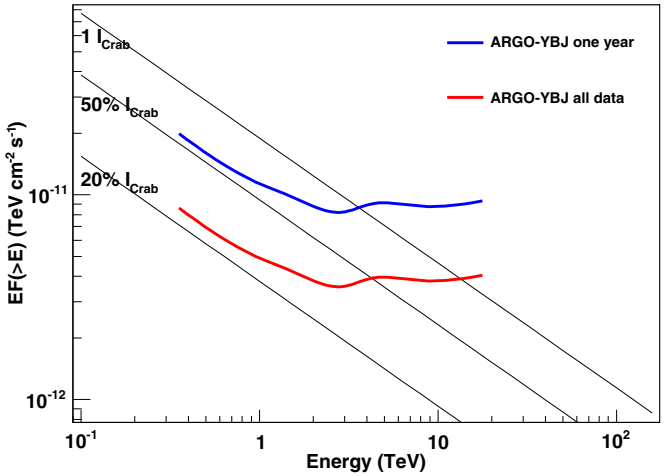

Figure 6. Sensitivity curve of the ARGO-YBJ detector estimated using its observation results on the Crab Nebula. The integrated sensitivity curve is obtained using five years of ARGO-YBJ data. The one-year sensitivity curve is scaled from this result. The duty cycle of the ARGO-YBJ detector has been taken into account.

(A color version of this figure is available in the online journal.)

Bartoli et al. (2012a) and are found to be less than 30%. As a standard candle, the Crab Nebula is used to estimate the sensitivity of an experiment. The 5 s.d. one-year sensitivity and the integrated sensitivity of ARGO-YBJ are shown in Figure 6. Events with $N_{\rm pad} \geqslant 20$, $N_{\rm pad} \geqslant 40$, etc., are used for this estimation. The integrated sensitivity using events with $N_{\rm pad} \geqslant 20$ is 24% $I_{\rm crab}$ and the corresponding one-year sensitivity is 55% $I_{\rm crab}$. The sensitivity decreases as energy increases. The integrated sensitivity is about 1 $I_{\rm crab}$ above an energy of 20 TeV.

ARGO J1105+3821, detected at 14 s.d., is consistent in position with the blazar Mrk 421. This is an active source and many outbursts have been detected by ARGO-YBJ over the past five years (Aielli et al. 2010; Bartoli et al. 2011a; Chen 2013). Its five-year average SED in the energy range from 0.1 TeV to 11 TeV is $dN/dE = (1.35 \pm 0.12) \times 10^{-11}(E/1\ \mathrm{TeV})^{-2.75\pm0.09}$ (TeV^{-1} cm^{-2} s^{-1}). The integral flux above 1 TeV is $(1.30 \pm 0.11) \times 10^{-11}$ cm^{-2} s^{-1}, corresponding to $\sim$0.70 $I_{\rm Crab}$.

ARGO J1654+3945, detected at 9 s.d., is consistent in position with the blazar Mrk 501. This source entered into an active phase in 2011 October, according to ARGO-YBJ observations (Bartoli et al. 2012b). Its five-year average SED in the energy range from 0.2 TeV to 12 TeV is $dN/dE = (1.01 \pm 0.11) \times 10^{-11}(E/1\ \mathrm{TeV})^{-2.37\pm0.18}$ (TeV^{-1} cm^{-2} s^{-1}). The integral flux above 1 TeV is $(0.95 \pm 0.10) \times 10^{-11}$ cm^{-2} s^{-1}, corresponding to $\sim$0.51 $I_{\rm Crab}$.

ARGO J1839−0627 is an extended source. Most of the excess overlaps the extended region of the unidentified source HESS J1841−055 even if the peak position is slightly displaced from the center of HESS J1841−055 (Aharonian et al. 2008a). The morphology detected by H.E.S.S. exhibits a highly extended, possibly two- or three-peaked region. A similar morphology is also detected by ARGO-YBJ using events $N_{\rm pad} > 100$ as shown in Figure 4. Parameterizing the source shape with a two-dimensional Gaussian function, the extension is estimated to be $\sigma = (0.40^{+0.32}_{-0.22})^{\circ}$, which is consistent with the H.E.S.S. measurement. The flux measured by ARGO-YBJ is higher than that determined by H.E.S.S. by a factor of $\sim$3. A detailed discussion about this object can be found in Bartoli et al. (2013). Recently, a young energetic γ-ray pulsar PSR J1838−0537 has been detected within its extended region (Pletsch et al. 2012). The inferred energetics suggests that HESS J1841−055 may contain a pulsar wind nebula powered by the pulsar.

ARGO J1907+0627 is closely connected to *ARGO J1910+0720*. ARGO J1907+0627 is consistent in position with HESS J1908+063 (Aharonian et al. 2009), while ARGO J1910+0720 is completely outside the extended region of HESS J1908+063. In a previous work, these two sources have been considered as a single unique source, identified as the extended source MGRO J1908+06 with an extension of $\sigma = 0.^{\circ}49 \pm 0.^{\circ}22$ (Bartoli et al. 2012c). The flux determined by ARGO-YBJ was consistent with that of Milagro but higher than that of HESS by a factor of $\sim$3. Its extended size is also marginally larger than the H.E.S.S. result. Therefore, MGRO J1908+06 could be a blend of the two sources. ARGO J1907+0627 is consistent in position with the pulsar PSR J1907+0602, and could be the associated pulsar wind nebula. Very close to ARGO J1910+0720, a counterpart in the hard X-ray band, SWIFT J1910.8+0739(4U 1909+07) (R.A. = $287.^{\circ}699$, decl. = $7.^{\circ}598$ in J2000 epoch) (Tueller et al. 2010), is located. This X-ray source is a high-mass X-ray binary (HMXB), a type of source identified as a VHE γ-ray emitter. ARGO J1910+0720 is detected at only 4.3 s.d., and the nearby source ARGO J1907+0627 could contribute to the observed excess. With the current statistics, we cannot exclude the possibility of a background fluctuation. However, this is an interesting region for follow-up observations with more sensitive instruments.

ARGO J1912+1026, detected at 4.2 s.d., is consistent in position with HESS J1912+101 (Aharonian et al. 2008b). HESS J1912+101 is an extended source with an intrinsic Gaussian width $0.^{\circ}26 \pm 0.^{\circ}03$ assuming a symmetrical two-dimensional Gaussian shape. Assuming a power-law spectrum, the spectral index obtained by ARGO-YBJ is -2.68 ± 0.35, which is consistent with -2.7 ± 0.2 obtained by H.E.S.S. However, the flux above 1 TeV is 23% $I_{\rm Crab}$, much higher than the value of 9% $I_{\rm Crab}$ determined by H.E.S.S. We reported a similar disagreement for the source HESS J1841-055 and MGRO J1908+06. Further discussion for such a discrepancy can be found in Bartoli et al. (2013).

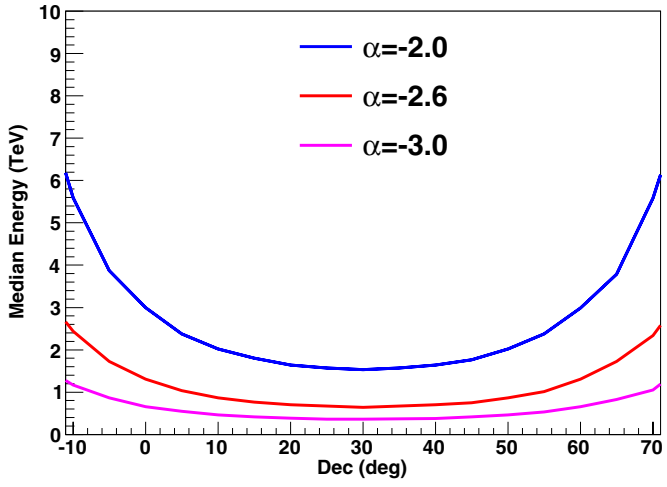

Figure 7. Median energy of all the γ-ray events that trigger ARGO-YBJ ($N_{\rm pad} \geqslant 20$) and satisfy the event selections, as a function of the source declination. Different lines correspond to different spectral indices, i.e., −2.0, −2.6, and −3.0.

(A color version of this figure is available in the online journal.)

ARGO J2021+4038, in the Cygnus region, is consistent in position with VER J2019+407 (Aliu et al. 2013), whose flux is only 3.7% $I_{\rm Crab}$, but the nearby extended source ARGO J2031+4157 could contribute to most of the excess, as shown in Figure 4.

ARGO J2031+4157 is a highly extended source located in the Cygnus region, consistent in position with MGRO J2031+41 and TeV J2032+4130. The intrinsic extension estimated using ARGO-YBJ data is $\sigma = (0.2^{+0.4}_{-0.2})^\circ$ (Bartoli et al. 2012a). In this case, the measured flux is also higher than that measured by IACTs, but with a discrepancy of more than a factor 10. A detailed report on this region can be found in Bartoli et al. (2012a). This region is also positionally consistent with the cocoon of freshly accelerated cosmic rays detected by *Fermi* (Ackermann et al. 2011b).

ARGO J0409−0627, detected at 4.8 s.d., is outside the Galactic plane. No counterpart at lower energies, including GeV γ-ray and X-ray bands, has previously been found. Its post-trial significance is the lowest among the sources listed in Table 2 and is less than 3 s.d.

ARGO J1841−0332 is detected at 3.4 s.d. using events $N_{\rm pad} \geqslant 20$ and at 4.2 s.d. using events $N_{\rm pad} \geqslant 100$. This source is observed at high zenith angles, where large systematic pointing errors are expected, therefore, it is likely coincident with the VHE γ-ray source HESS J1843−033, even though it is displaced by 0.°7. Five other GeV γ-ray sources surround this region, as shown in Figure 4. An observation with improved sensitivity is necessary to clarify this possible TeV emission.

4.3. Sky Upper Limits

Excluding the sources listed in Table 2, we can set upper limits to the γ-ray flux from all the directions in the observed sky region.

To estimate the response of the ARGO-YBJ detector, we simulate a source located at different declinations with a power-law spectrum in the energy range from 10 GeV to 100 TeV. Each source is traced by means of a complete transit, i.e., 24 hr of observation. Figure 7 shows the median energy of all γ-induced showers that trigger ARGO-YBJ, i.e., $N_{\rm pad} \geqslant 20$, and satisfy the event selections for sources with different spectral indices. When the index is −2.6, similar to that of the Crab Nebula, the median energy varies from 0.64 TeV at decl. = 30° (the latitude of ARGO-YBJ) to 2.4 TeV at decl. = −10° and decl. = 70°. For sources with a hard spectral index −2.0, the corresponding range of median energy is from 1.5 TeV to 5.6 TeV. The median energy varies from 0.36 TeV to 1.1 TeV for sources with a soft spectral index −3.0.

The statistical method given in Helene (1983) is used to calculate the upper limit on the number of signal events at 95% C.L. in each bin. The number of events is transformed into a flux using the results of the simulation. The upper limits to the flux of γ-rays with energies above 500 GeV for each bin are shown in Figure 8. The spectral index is assumed to be −2.6. The average upper limits, as a function of the declination, are shown in Figure 9. The limits range between 9% and 44% $I_{\rm Crab}$ and are the lowest obtained so far. The lowest limit for a spectral index −2.0 (−3.0) is 5% (9%) $I_{\rm Crab}$, as shown in Figure 9.

The flux upper limits shown in Figures 8 and 9 are for point sources. For extended sources, the corresponding flux upper limit will increase. For a symmetrical two-dimensional Gaussian shape with $\sigma = 0.^\circ2$, the upper limit will increase by 10%. If $\sigma = 0.^\circ3$ and $\sigma = 0.^\circ5$, the increase will be of 20% and 44%, respectively. For this estimation, we assumed a spectral index −2.6.

With an energy threshold lower than any other previous EAS array, ARGO-YBJ is suitable for the observation of AGNs, the dominant γ-ray extragalactic sources. For an extragalactic source, the absorption of γ-rays due to the interaction with the EBL must be taken into account. By choosing the model proposed in Franceschini et al. (2008), the effect of EBL absorption on the upper limits has been evaluated, and the absorption factors with respect to a source with redshift $z = 0$ are shown in Figure 10, for a source spectral index of −2.6. Curves for redshift values of 0.03, 0.06, 0.1, and 0.3 are shown. The flux upper limits shown in Figure 8, multiplied by the absorption factor shown in Figure 10, give the unabsorbed flux upper limit at the source. The values of the absorption factors are about 1.5–2.2 for sources with a redshift $z = 0.03$, and increase by a factor of ∼10 for sources at $z = 0.3$. The absorption is stronger (weaker) for sources with harder (softer) spectra. Figure 11 shows examples of the absorption factors for sources with spectral indices of −2 and −3.

According to the *Fermi*-LAT second AGN catalog (2LAC), 663 AGNs are within the ARGO-YBJ FOV (Ackermann et al. 2011a). Figure 12 shows the comparison of ARGO-YBJ flux upper limits with the fluxes obtained by extrapolating to TeV energies the SEDs measured by *Fermi*-LAT in the range 1–100 GeV. The extrapolation is performed assuming that the spectral index steepens by 0.5 at 100 GeV. This spectral behavior is physically motivated because radiative cooling is expected to modify the electron power-law index by 1 and the corresponding γ-ray index by 0.5. For convenience, we show in Figure 12 the differential fluxes at 1 TeV. As can be seen, for 135 AGNs out of the total 663, the calculated upper limits are lower than the extrapolated fluxes, suggesting steeper spectra above 100 GeV. Such an effect could be due to the absorption of photons by the EBL, since the average redshift is 0.27 for BL Lac objects and 1.12 for FSRQs (Ackermann et al. 2011a). As evident from Figures 10 and 11, the absorption factors are very high. The redshift has been measured for 68 AGNs out of 135. Figure 13 shows the upper limits taking into account the EBL absorption. For 10 sources out of 68, the limits set in this work constrain the intrinsic spectra to have steeper slopes. These AGNs are listed in Table 3, which also reports the index measured by *Fermi* in the

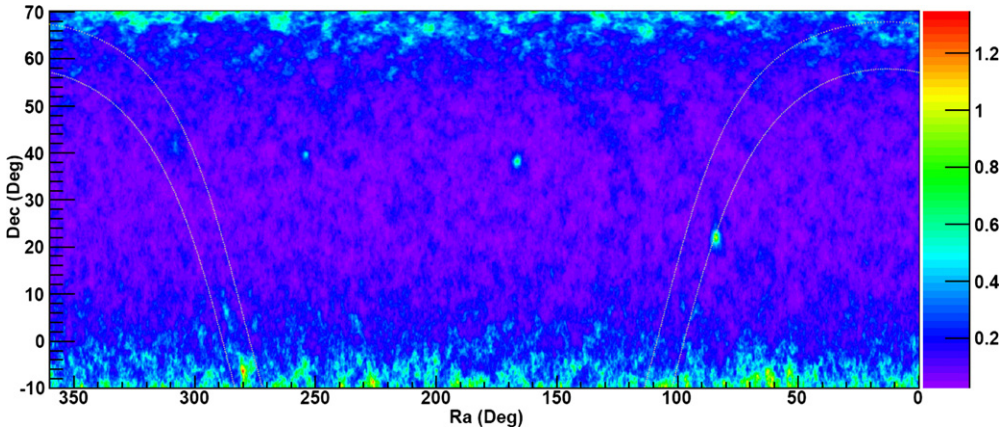

Figure 8. Map of the 95% C.L. flux upper limits at energies above 500 GeV assuming an energy spectrum $E^{-2.6}$. The color scale on the right is in Crab units, i.e., 5.69×10^{-11} cm^{-2} s^{-1}. The two dotted lines indicate the Galactic latitudes $b = \pm 5^{\circ}$.

(A color version of this figure is available in the online journal.)

Table 3
ARGO-YBJ Upper Limits for Sources in the 2LAC

Name (2FGL)	Associated TeV Source	R.A.[a] (deg)	Decl.[a] (deg)	z	Index[b]	Flux[c]	Upper Limit[d]	S (s.d.)
J0319.8+4130	NGC 1275	49.950	41.512	0.018	2.00	1.95e−11	5.31e−12	1.4
J1015.1+4925	1ES 1011+496	153.767	49.434	0.212	1.72	3.96e−11	3.23e−11	−0.5
J1104.4+3812	Mrk 421	166.114	38.209	0.031	1.77	1.15e−10[e]	2.82e−11	13.9
J1117.2+2013		169.276	20.235	0.138	1.70	1.07e−11	8.77e−12	−1.8
J1428.6+4240	H 1426+428	217.135	42.673	0.129	1.32	3.49e−11	1.72e−11	0.2
J1653.9+3945	Mrk 501	253.468	39.760	0.034	1.74	4.09e−11[f]	2.02e−11	9.1
J1744.1+1934	1ES 1741+196	265.991	19.586	0.083	1.62	5.82e−12	3.99e−12	−2.0
J2039.6+5218		309.848	52.331	0.053	1.50	6.95e−12	4.25e−12	−1.1
J2323.8+4212		350.967	42.183	0.059	1.88	5.09e−12	4.42e−12	−0.7
J2347.0+5142	1ES 2344+514	356.771	51.705	0.044	1.72	8.20e−12	4.50e−12	−0.8

Notes.
[a] R.A. and decl. are celestial coordinates in J2000 epoch quoted in the 2LAC (Ackermann et al. 2011a).
[b] The power-law spectral index reported in the 2LAC (Ackermann et al. 2011a).
[c] Extrapolated differential flux at 1 TeV in units of TeV^{-1} cm^{-2} s^{-1} based on 2LAC parameters (Ackermann et al. 2011a).
[d] 95% C.L. flux upper limits at 1 TeV in units of TeV^{-1} cm^{-2} s^{-1}.
[e] The measured flux is 1.35e−11 and the corresponding un-absorbed flux is 2.07e−11.
[f] The measured flux is 1.01e−11 and the corresponding un-absorbed flux is 1.61e−11.

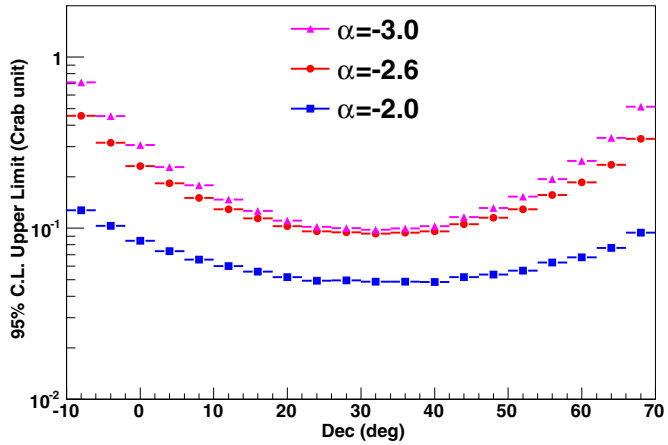

Figure 9. 95% C.L. flux upper limits at energies above 500 GeV averaged on the right ascension as a function of the declination. Different curves correspond to different power-law spectral indices −2.0, −2.6, and −3.0. The Crab unit is 5.69×10^{-11} cm^{-2} s^{-1}.

(A color version of this figure is available in the online journal.)

range 1–100 GeV, the differential flux extrapolated to 1 TeV, and the flux upper limits corrected for the absorption. Note that Mrk 421 and Mrk 501 have been significantly detected by ARGO-YBJ, and they are the two brightest AGNs. Five AGNs out of eight have been detected by IACTs as VHE γ-ray sources, and the spectra are consistent with the upper limits obtained here.

The upper limits obtained here for AGNs represent the five-year averaged flux. It is well known that many AGNs exhibit strong variability (up to a factor of 10) on different timescales. The upper limits for short periods are beyond the scope of this paper.

5. SUMMARY

This paper has presented the most sensitive survey to date of the sky in the declination band from -10° to 70° obtained with five years of ARGO-YBJ data. With an integrated sensitivity ranging from 0.24 to ∼1 Crab flux, depending on the declination, six sources have been observed with a statistical significance greater than 5 s.d. These sources are associated with well known TeV γ-ray emitters. Evidence for possible TeV emission from five directions is also reported. Two of these

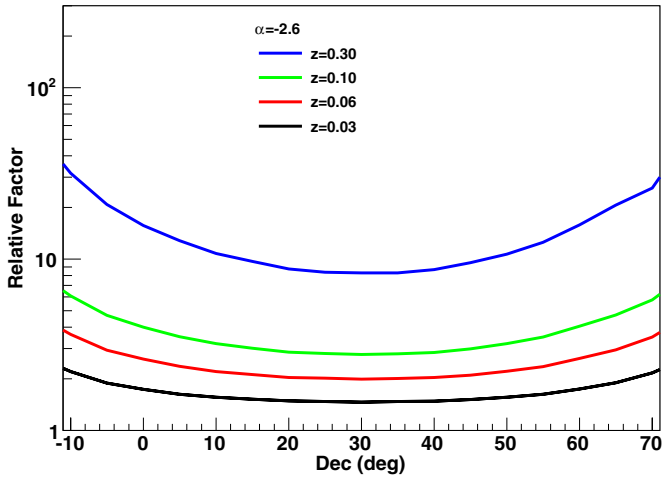

Figure 10. Effect of the EBL absorption on the upper limits shown in Figures 8 and 9. The source spectrum is assumed to be $E^{-2.6}$. The *y*-axis gives the absorption factor for a source at the indicated redshift relative to a source at redshift zero as a function of the declination.

(A color version of this figure is available in the online journal.)

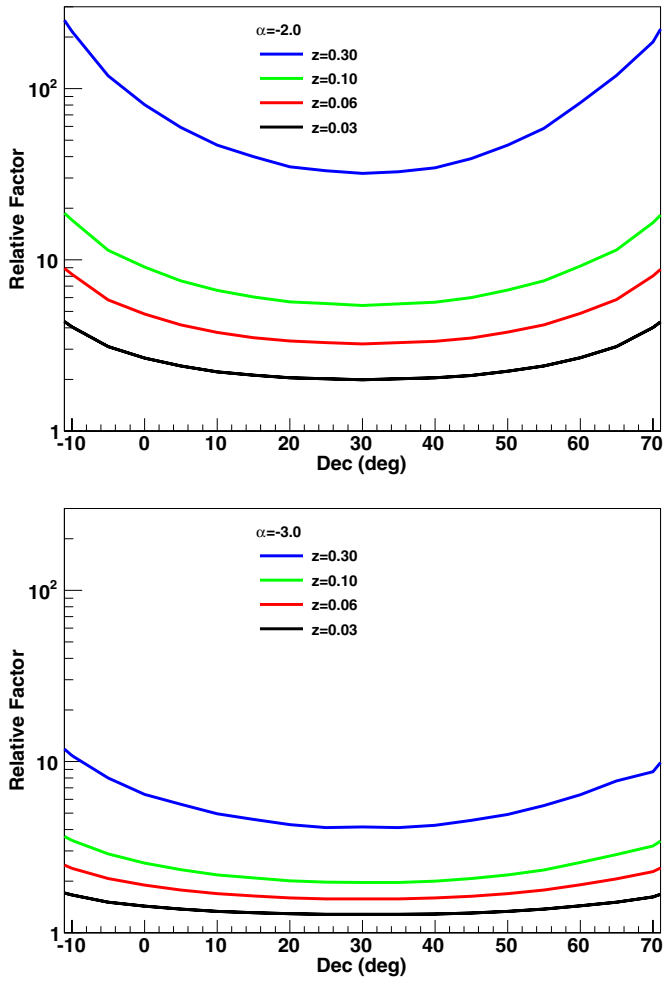

Figure 11. Effect of the EBL absorption on the upper limits shown in Figures 8 and 9. The source spectrum is assumed to be E^{-2} (top panel) and E^{-3} (bottom panel). The *y*-axis gives the absorption factor for a source at the indicated redshift relative to a source at redshift zero as a function of the declination.

(A color version of this figure is available in the online journal.)

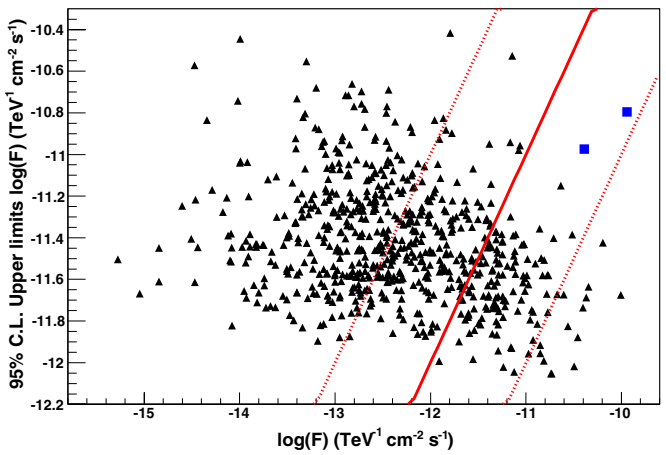

Figure 12. Comparison between ARGO-YBJ 95% C.L. flux upper limits and the expected flux for the 663 *Fermi*-LAT AGNs within the ARGO-YBJ FOV. The expected fluxes are obtained by extrapolating the SEDs measured by *Fermi*-LAT to TeV energies, assuming that the spectral index steepens by 0.5 at 100 GeV. Both fluxes are differential at 1 TeV. The solid line indicates where the upper limit equals the expected flux. The dotted lines indicate the 0.1 and 10 times relations between these two fluxes. All the upper limits are estimated assuming the source at redshift zero. The two squares correspond to Mrk 421 and Mrk 501.

(A color version of this figure is available in the online journal.)

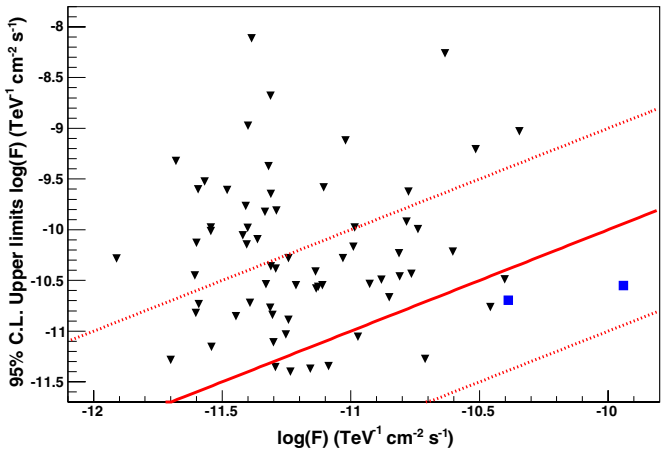

Figure 13. Comparison between ARGO-YBJ 95% C.L. flux upper limits and the expected flux for 68 *Fermi*-LAT AGNs with measured redshift. The expected fluxes are obtained by extrapolating the SEDs measured by *Fermi*-LAT to TeV energies, assuming that the spectral index steepens by 0.5 at 100 GeV. Both fluxes are differential at 1 TeV. The effect of the EBL absorption on the flux upper limits has been taken into account. The lines represent the same flux relations as in Figure 12. The two squares correspond to Mrk 421 and Mrk 501.

(A color version of this figure is available in the online journal.)

five excesses are not associated with any known counterpart and thus are potentially new TeV emitters. Of particular interest is the candidate source ARGO J1910+0720, which is coincident in position with a HMXB. The 95% C.L. upper limit to the γ-ray flux from all the directions in the mentioned declination band are also reported. The integral flux limits above 500 GeV vary from 0.09 to 0.44 Crab units for a Crab-like source, depending on the declination. The limits set by ARGO-YBJ in this work are the lowest available to date. Specific upper limits for 663 GeV AGNs are also presented and 8 AGNs are found with intrinsic spectra steeper than expected.

This work is supported in China by NSFC (Nos. 10120130794 and 11205165), the Chinese Ministry of Science and

Technology, the Chinese Academy of Sciences, the Key Laboratory of Particle Astrophysics, CAS, and in Italy by the Istituto Nazionale di Fisica Nucleare (INFN).

We also acknowledge the essential support of W. Y. Chen, G. Yang, X. F. Yuan, C. Y. Zhao, R. Assiro, B. Biondo, S. Bricola, F. Budano, A. Corvaglia, B. D'Aquino, R. Esposito, A. Innocente, A. Mangano, E. Pastori, C. Pinto, E. Reali, F. Taurino, and A. Zerbini, in the installation, debugging, and maintenance of the detector.

REFERENCES

Abdo, A. A., Allen, B., Berley, D., et al. 2007, ApJL, 664, L91
Abdo, A. A., Allen, B. T., Aune, T., et al. 2009, ApJL, 700, L127
Ackermann, M., Ajello, M., Allafort, A., et al. 2011a, ApJ, 743, 171
Ackermann, M., Ajello, M., Allafort, A., et al. 2011b, Sci, 334, 1103
Aharonian, F., Akhperjanian, A., Barrio, J. A., et al. 2002, A&A, 390, 39
Aharonian, F., Akhperjanian, A., Beilicke, M., et al. 2004, ApJ, 614, 897
Aharonian, F., Akhperjanian, A. G., Anton, G., et al. 2009, A&A, 499, 723
Aharonian, F., Akhperjanian, A. G., Barres de Almeida, U., et al. 2008a, A&A, 477, 353
Aharonian, F., Akhperjanian, A. G., Barres de Almeida, U., et al. 2008b, A&A, 484, 435
Aharonian, F., Akhperjanian, A. G., Bazer-Bachi, A. R., et al. 2006, A&A, 457, 899
Aharonian, F., Buckley, J., Kifune, T., & Sinnis, G. 2008c, RPPh, 71, 096901
Aielli, G., Assiro, R., Bacci, C., et al. 2006, NIMPA, 562, 92
Aielli, G., Bacci, C., Barone, F., et al. 2009a, ApJ, 699, 1281
Aielli, G., Bacci, C., Bartoli, B., et al. 2009b, APh, 30, 287
Aielli, G., Bacci, C., Bartoli, B., et al. 2009c, APh, 32, 47
Aielli, G., Bacci, C., Bartoli, B., et al. 2009d, NIMPA, 608, 246
Aielli, G., Bacci, C., Bartoli, B., et al. 2010, ApJL, 714, L208
Aielli, G., Bacci, C., Bartoli, B., et al. 2011, ApJ, 729, 113
Albert, J., Aliu, E., Anderhub, H., et al. 2008a, Sci, 320, 1752
Albert, J., Aliu, E., Anderhub, H., et al. 2008b, ApJ, 674, 1037
Aliu, E., Archambault, S., Arlen, T., et al. 2013, ApJ, 770, 93
Amenomori, M., Ayabe, S., Chen, D., et al. 2005, ApJ, 633, 1005
Amenomori, M., Bi, X. J., Chen, D., et al. 2009, ApJ, 692, 61
Amenomori, M., Bi, X. J., Chen, D., et al. 2010, ApJL, 709, L6
Atkins, R., Benbow, W., Berley, D., et al. 2004, ApJ, 608, 680
Bartoli, B., Bernardini, P., Bi, X. J., et al. 2011a, ApJ, 734, 110
Bartoli, B., Bernardini, P., Bi, X. J., et al. 2011b, PhRvD, 84, 022003
Bartoli, B., Bernardini, P., Bi, X. J., et al. 2012a, ApJL, 745, L22
Bartoli, B., Bernardini, P., Bi, X. J., et al. 2012b, ApJ, 758, 2
Bartoli, B., Bernardini, P., Bi, X. J., et al. 2012c, ApJ, 760, 110
Bartoli, B., Bernardini, P., Bi, X. J., et al. 2013, ApJ, 767, 99
Capdevielle, J. N., Grieder, P., Knapp, J., et al. 1992, KfK Report No. 4998
Chen, S. Z. 2013, ScChG, 56, 1454
Eckmann, R., Haustein, V., Heinzelmann, G., & Prahl, J. 1991, in Proc. 22nd ICRC, Vol. 4, High Energy Phenomena, ed. M. Cawley et al. (Dublin: IUPAP), 464
Fleysher, R., Fleysher, L., Nemethy, P., & Mincer, A. I. 2004, ApJ, 603, 355
Franceschini, A., Rodighiero, G., & Vaccari, M. 2008, A&A, 487, 837
Gast, H., Brun, F., Carrigan, S., et al. 2011, in Proc. of 32nd ICRC, Vol. 7, OG Cosmic Ray Origin and Galactic Phenomena (Beijing: IUPAP), 158
Guo, Y. Q., Zhang, X.-Y., Zhang, J.-L., et al. 2010, ChPhC, 34, 555
Hartman, R. C., Bertsch, D. L., Bloom, S. D., et al. 1999, ApJS, 123, 79
He, H. H., Bernardini, P., Calabrese Melcarne, A. K., & Chen, S. Z. 2007, APh, 27, 528
Helene, O. 1983, NIMPR, 212, 319
Li, T. P., & Ma, Y. Q. 1983, ApJ, 272, 317
Nolan, P. L., Abdo, A. A., Ackermann, M., et al. 2012, ApJS, 199, 31
Pletsch, H. J., Guillemot, L., Allen, B., et al. 2012, ApJL, 755, L22
Tueller, J., Baumgartner, W. H., Markwardt, C. B., et al. 2010, ApJS, 186, 378